Spitzer thermal phase curve of WASP-121 b

(article starts on next page)

Spitzer thermal phase curve of WASP-121 b

G. Morello[1,2] , Q. Changeat[3,4] , A. Dyrek[5] , P.-O. Lagage[5], and J. C. Tan[1,6]

[1] Department of Space, Earth and Environment, Chalmers University of Technology, 412 96 Gothenburg, Sweden
[2] Instituto de Astrofísica de Canarias (IAC), Vía Láctea, s/n, 38205 La Laguna, Tenerife, Spain
  e-mail: `giuseppe.morello-ext@iac.es`
[3] European Space Agency (ESA), ESA Office, Space Telescope Science Institute (STScI), Baltimore, MD 21218, USA
[4] Department of Physics and Astronomy, University College London, Gower Street,WC1E 6BT London, UK
[5] AIM, CEA, CNRS, Université Paris-Saclay, Université Paris-Diderot, Sorbonne Paris-Cité, 91191 Gif-sur-Yvette, France
[6] Dept. of Astronomy, University of Virginia, 530 McCormick Rd, Charlottesville, VA 22904, USA

ABSTRACT

Aims. We analyse unpublished *Spitzer* observations of the thermal phase-curve of WASP-121 b, a benchmark ultra-hot Jupiter.
Methods. We adopted the wavelet pixel-independent component analysis technique to remove challenging instrumental systematic effects in these datasets and we fit them simultaneously with parametric light-curve models. We also performed phase-curve retrievals to better understand the horizontal and vertical thermal structure of the planetary atmosphere.
Results. We measured planetary brightness temperatures of ∼2700 K (dayside) and ∼700–1100 K (nightside), along with modest peak offsets of $5.9° ± 1.6$ (3.6 μm) and $5.0°^{+3.4}_{-3.1}$ (4.5 μm) after mid-eclipse. These results suggest inefficient heat redistribution in the atmosphere of WASP-121 b. The inferred atmospheric Bond albedo and circulation efficiency align well with observed trends for hot giant exoplanets. Interestingly, the measured peak offsets correspond to a westward hot spot, which has rarely been observed. We also report consistent transit depths at 3.6 and 4.5 μm, along with updated geometric and orbital parameters. Finally, we compared our *Spitzer* results with previous measurements, including recent JWST observations.
Conclusions. We extracted new information on the thermal properties and dynamics of an exoplanet atmosphere from an especially problematic dataset. This study probes the reliability of exoplanet phase-curve parameters obtained from *Spitzer* observations when state-of-the-art pipelines are adopted to remove the instrumental systematic effects. It demonstrates that *Spitzer* phase-curve observations provide a useful baseline for comparison with JWST observations, and shows the increase in parameters precision achieved with the newer telescope.

Key words. planetary systems – planets and satellites: individual: WASP-121 b – planets and satellites: atmospheres – techniques: spectroscopic – methods: observational

1. Introduction

WASP-121 b is an ultra-hot Jupiter (UHJ) orbiting around an F6 V star in ∼1.27 d. Table 1 reports the stellar and planetary parameters taken from its discovery paper (Delrez et al. 2016). WASP-121 b has been targeted by many follow-up studies, based on its nature as an exoplanet amenable to characterisations with various observing techniques. It is especially well suited for atmospheric characterisation by both transmission and emission spectroscopy, owing to its high equilibrium temperature and large size. Some researchers have proposed WASP-121 b as a suitable target to further investigate its interior structure and/or shape deformations (Akinsanmi et al. 2019; Hellard et al. 2020).

Shortly after the WASP-121 b discovery, Evans et al. (2016) detected the 1.4 μm water absorption band from a transit observed with the *Hubble* Space Telescope (HST) using the Wide Field Camera 3 (WFC3) with the G141 grism, covering 1.1–1.7 μm. Evans et al. (2017) also detected H_2O in emission, along with evidence of a stratosphere, using the same instrument setup to observe the planetary eclipse. Earlier atmospheric models of UHJs predicted temperature inversions to occur due to absorption by metal oxides, such as TiO and VO, in their upper atmospheric layers (Hubeny et al. 2003; Fortney et al. 2008). Small features occurring at the blue edge of the HST/WFC3 spectra of WASP-121 b have been tentatively attributed to TiO and VO (Evans et al. 2017; Tsiaras et al. 2018). Based on subsequent transit observations obtained with the HST/Space Telescope Imaging Spectrograph (STIS), covering 0.3–1.0 μm, Evans et al. (2018) confirmed the presence of VO, but not TiO, at the terminator of WASP-121 b atmosphere. Mikal-Evans et al. (2019) found evidence of H^- in the emission spectrum of WASP-121 b taken with HST/WFC3 using the G102 grism (0.8–1.1 μm), but retracted the previous claim of VO in emission. Mikal-Evans et al. (2020) refined H_2O detection and VO non-detection in the planet dayside by stacking multiple eclipse observations taken with HST/WFC3 G141. Salz et al. (2019) detected an excess of near-UV absorption (0.20–0.27 μm) during three transits of WASP-121 b observed with the Ultraviolet/Optical Telescope (UVOT) onboard the *Neil Gehrels Swift* Observatory. Sing et al. (2019) resolved exospheric Mg II and Fe II lines in the near-UV transmission spectrum observed with HST/STIS.

Bourrier et al. (2020) and Daylan et al. (2021) reported two independent analyses of long-term visible photometry of WASP-121 from the Transiting Exoplanet Survey Satellite (TESS; Ricker et al. 2014) showing strong phase-curve modulations. Both studies measured a strong day-night temperature contrast and a small offset between the maximum emission and substellar points, suggesting low reflectivity and inefficient heat redistribution in the planetary atmosphere. They also found evidence

Table 1. WASP-121 system parameters.

Stellar parameters	
$T_{*,\mathrm{eff}}$ (K)	6460 ± 140
$\log g_*$ (cgs)	4.2 ± 0.2
[Fe/H]$_*$ (dex)	0.13 ± 0.09
M_* ($M_\odot$)	1.35 ± 0.08
R_* ($R_\odot$)	1.46 ± 0.03
Planetary parameters	
M_p (M_Jup)	1.18 ± 0.06
R_p (R_Jup)	1.81 ± 0.04
$T_\mathrm{p,eq}$ (K)	2358 ± 52
a (au)	0.02544 ± 0.00050
P (day)	$1.2749255^{+2.0 \times 10^{-7}}_{-2.5 \times 10^{-7}}$
T_0 (HJD$_\mathrm{TDB}$)	$2\,456\,636.34578^{+0.00011}_{-0.00010}$

Notes. From Delrez et al. (2016).

for a temperature inversion, partly caused by H⁻. Mikal-Evans et al. (2022) analysed two spectroscopic phase curves observed with HST/WFC3 G141, revealing variations in the H_2O feature that correspond to a thermal profile warming (cooling) with altitude in the dayside (nightside). These data are consistent with models predicting thermal dissociation of H_2O on the dayside and recombination on the nightside (Parmentier et al. 2018). The *James Webb* Space Telescope (JWST) has recently observed a full phase curve of WASP-121 b using the Near-InfraRed Spectrograph (NIRSpec) with the G395H grism (2.70–5.15 μm). Mikal-Evans et al. (2023) published their first-look analysis of the JWST/NIRSpec data, the results of which align well with those in the previous literature.

WASP-121 b has also been the subject of numerous ground-based observing campaigns. Kovács & Kovács (2019) detected a deep planetary eclipse in the 2MASS K band with A Novel Dual Imaging CAMera (ANDICAM) attached to the 1.3-m telescope of the SMARTS Consortium. Multiple studies based on the high-resolution Doppler spectroscopy technique placed severe upper limits on the possible presence of TiO and VO in gaseous form (e.g. Merritt et al. 2020; Hoeijmakers et al. 2020). However, the high-resolution spectra revealed a rich inventory of metals and ions in the WASP-121 b atmosphere, including Hα, Na I, Fe I, Fe II, Cr I, V I, Mg I, Ni I, Ca I, Ca II, K I, Li I, Sc II, Ba II, Co I, and Sr II (Ben-Yami et al. 2020; Cabot et al. 2020; Hoeijmakers et al. 2020; Borsa et al. 2021; Merritt et al. 2021; Azevedo Silva et al. 2022).

In this paper, we present the first analysis of two phase curves of WASP-121 b observed with the *Spitzer*/InfraRed Array Camera (IRAC) channels 1 and 2 (Fazio et al. 2004), which operate in photometric passbands centred at 3.6 and 4.5 μm, respectively. These data were acquired by the end of January 2018 for the *Spitzer* program ID 13242 (PI: Tom Evans). Using the wavelet pixel-independent component analysis (ICA) pipeline (Morello et al. 2016), we overcome the issues of strong instrumental systematic effects that may have prevented their publication so far. We validate the robustness of our results, comparing them with those from recent JWST observations in similar passbands.

Section 2 presents the *Spitzer*/IRAC observations of WASP-121 b phase curves. Section 3 describes the procedure adopted in this work to analyse the data. Section 4 reports our results, including the transit and phase-curve parameters, and derived

atmospheric properties. Section 5.1 discusses the atmospheric properties of WASP-121 b with more details, including the results of phase-curve retrievals. Section 5.2 compares our results with those from previous observations to obtain a more complete picture of the atmosphere of WASP-121 b, and puts them in the context with other UHJs. Section 6 summarizes the conclusions of our study.

2. Observations

We analysed two phase curves of WASP-121 b observed with *Spitzer*/IRAC for the program ID 13242 (PI: Tom Evans). Each visit consists of four consecutive astronomical observation requests (AORs) spanning approximately 39 hr, including one transit and two eclipse events. The observations were taken using IRAC sub-array readout mode with 2 s frame time (Fazio et al. 2004). In this mode, 64 frames are taken consecutively, with a delay of 1.27 s after reset. In total, 69 184 frames were acquired per visit, split unequally across the four AORs, but analogously for the two visits. The first visit made use of IRAC channel 2, that is, photometric filter with ~4.0–5.0 μm passband and effective wavelength of 4.5 μm. The second visit made use of IRAC channel 1, that is, photometric filter with ~3.2–3.9 μm passband and effective wavelength of 3.6 μm. Table 2 summarises the main details of the observations.

3. Data analysis

3.1. Raw photometry extraction

We downloaded the basic calibrated data (BCD, files extension '_bcd.fits') from the *Spitzer* Heritage Archive (Wu et al. 2010). The BCD are flat-fielded and flux-calibrated frames (Fazio et al. 2004; IRAC Instrument & Instrument Support Teams 2021). We extracted the pixel time series from 5×5 arrays where the central pixel records the highest flux in most frames within an AOR. The raw light curves were computed as the sum of pixel time series from the 5x5 arrays. We note that the selected array could vary between AORs within the same visit. We also attempted to use a single array for each entire visit, but this choice increased the photometric offsets between AORs and degraded the performance of our data detrending method.

We flagged and corrected outliers in the raw light curves through the following procedure. First, we computed the smoothed reference light curves as the sliding window medians of binned raw light curves. We adopted a bin size of 64, corresponding to the original data cube size, and a sliding window size of five. Second, we computed the reference noise level for the unbinned raw light curves as the median of the moving standard deviation with a sliding window of five. Third, we identified outliers as those points that are more than 5σ away from the smoothed references. Fourth, we replaced the sets of consecutive outliers with the vector means of the adjacent sets, or, equivalently, via a linear interpolation in the case of isolated outliers. The replacements were applied to all pixel light curves, and not just to the raw light curves. We iterated the third and fourth steps until there were no outliers left in the raw light curves.

Finally, we binned all the light curves by a factor of four, corresponding to an integration time of 8 s, to speed up the following data analysis. The chosen bin size is a conservative one, being much smaller than the occultation timescales (Kipping 2010). We could have adopted a larger bin size for the parts outside the occultations, based on the phase curve

Table 2. *Spitzer*/IRAC datasets analysed for this study.

Filter [i]	Prog. ID	AORs [ii]	UT start date [iii]	N_{frames}	Mode [iv]	Pip. [v]
Ch1 (3.6 µm)	13242	64973056	2018-01-29 16:47:26	17536	sub, 2.0	S19.2.0
″	″	64974080	2018-01-30 02:42:12	9408	″	″
″	″	64973568	2018-01-30 08:03:03	21120	″	″
″	″	64975104	2018-01-30 19:58:36	21120	″	″
Ch2 (4.5 µm)	13242	64974592	2018-01-27 03:53:22	17536	sub, 2.0	S19.2.0
″	″	64972544	2018-01-27 13:48:00	9408	″	″
″	″	64974848	2018-01-27 19:08:43	21120	″	″
″	″	64972288	2018-01-28 07:04:09	21120	″	″

Notes. [i] IRAC channel and central wavelength. [ii]Astronomical observation requests. [iii]Timestamp of the first frame of the AOR. [iv]Readout mode and frame time in seconds. [v]Pipeline version of the basic calibrated data.
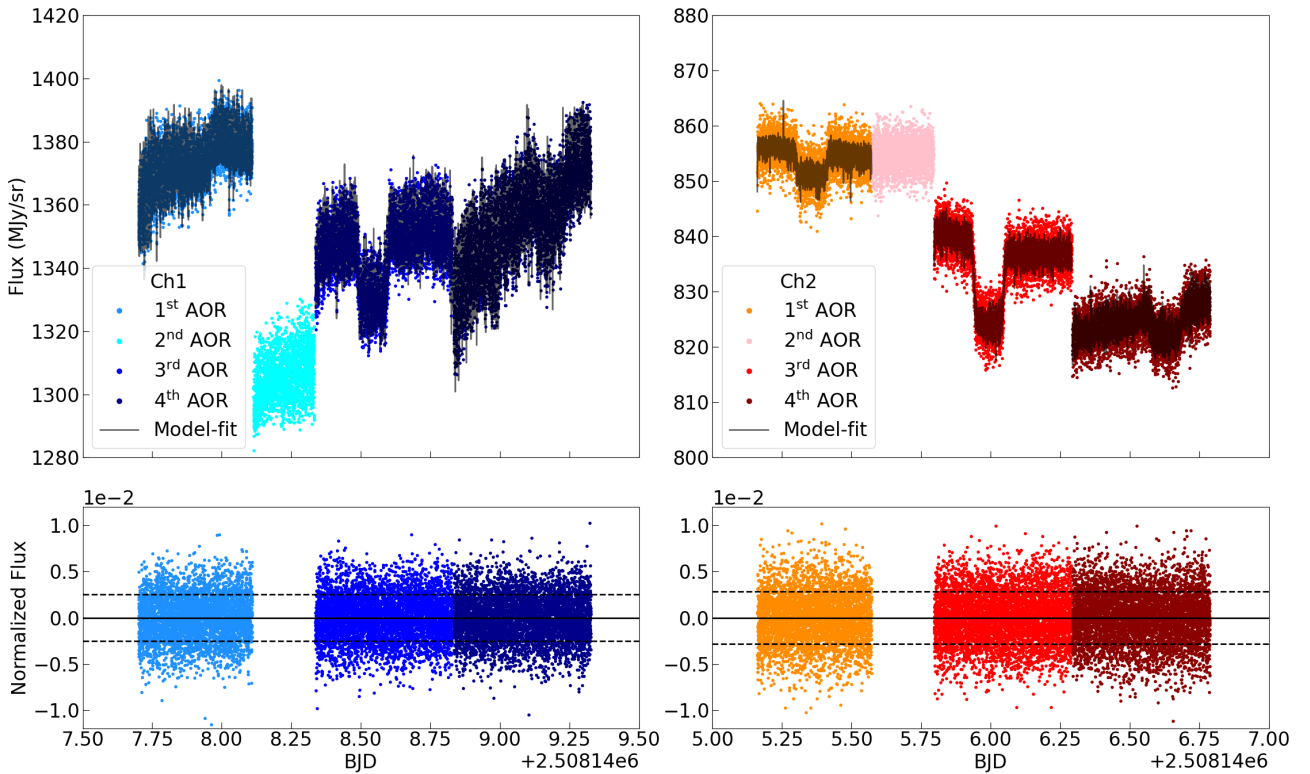

Fig. 1. Raw light curves obtained for the *Spitzer*/IRAC observations at 3.6 µm (left panel) and 4.5 µm (right panel), shown at the top and represented by dots of different colours for each AOR. The relevant best-fit models, including instrumental systematics, are overplotted with solid lines. Note that the second AOR of each visit was discarded from the light-curve fits. The bottom panels show residuals from the above light curves and models (dots), and standard deviations (black lines).

timescales, but our choice also minimizes the impact of correlated noise (Morello et al. 2022). Figure 1 shows the binned raw light curves analysed in this work.

For illustrative purposes only, we calculated the coordinates of the stellar centroid using the centre-of-light method, as implemented by Morello (2015). Figure 2 shows the x and y coordinates obtained for both visits. It appears by eye that the centroids describe different loci in the x–y plane for each AOR. Pointing is stable mostly within 1–2 tenths of the pixel side during an AOR, then jumps abruptly by up to more than half a pixel when starting a new AOR. The larger-than-usual discontinuities likely make these datasets especially challenging to analyse compared to other *Spitzer*/IRAC phase-curve observations (e.g. Stevenson et al. 2017; Morello et al. 2019).

3.2. Data detrending

We applied the wavelet pixel-ICA technique, which is one of the most efficient for detrending *Spitzer*/IRAC time series (Ingalls et al. 2016). ICA is a blind source separation technique with a wide range of applications, including many astrophysical fields (e.g. Maino et al. 2002, 2007; Wang et al. 2010, 2013; Chapman et al. 2012; Waldmann 2012, 2014; Waldmann et al. 2013; Damiano et al. 2017; Rodríguez-Montoya et al. 2018; Di Marcantonio et al. 2019). It performs a linear transformation of input mixed signals into maximally independent components (Hyvärinen 2001). The wavelet pixel-ICA technique uses wavelet-transformed pixel light curves as input for the ICA (Morello et al. 2016). It is an improvement on the pixel-ICA
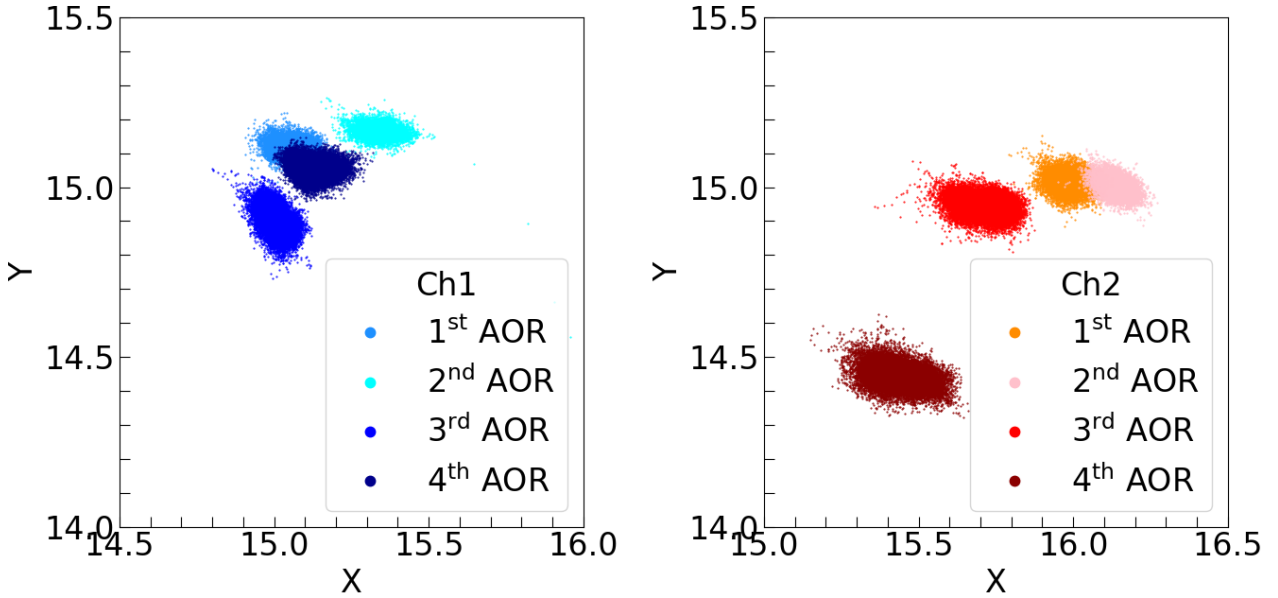
Fig. 2. Centroid coordinates of the *Spitzer*/IRAC images, using different colours for each AOR (as in Fig. 1). Note: there are pointing offsets of few tenths of pixels between consecutive AORs.

technique, which instead used pixel light curves in the time domain (Morello et al. 2014, 2015; Morello 2015). As in previous papers, here we applied a single-level discrete wavelet transform (DWT) to the pixel light curves, but adopting the Haar wavelet (Haar 1910) instead of the more complex Daubechies-4 one (Daubechies 1992). We checked, however, that the choice of wavelet function does not noticeably affect the ICA transform. The adopted ICA algorithm is MULTICOMBI (Tichavsky et al. 2008), as always. This time we wrapped the original MATLAB source code for use in a Python script.

We initially tried to concatenate the pixel light curves from multiple AORs to form a single set of input signals to be transformed with ICA for each visit. Morello et al. (2019) successfully adopted this approach to detrend *Spitzer*/IRAC phase curves of WASP-43 b. The same approach failed on the WASP-121 b data presented here, most likely due to larger pointing jumps between consecutive AORs. Therefore, we decided to perform individual ICA transforms for each AOR. We excluded the second AORs from each visit. In fact, these AORs do not contain an astrophysical signal with a well recognizable shape, such as a transit or an eclipse. The lack of morphology makes it difficult to separate the astrophysical component from the instrumental ones. For all other AORs, we identified the first ICA component as the astrophysical one, containing a clear transit or eclipse signal. Following the usual procedure, these astrophysical components were discarded from the light-curve fits, being replaced by an astrophysical light-curve model. The other 24 components of each AOR were attributed to instrumental systematic signals.

3.3. Light-curve models

Our phase-curve model approximates the planetary flux with a double sinusoid,

$$F_{\rm p} = c_0 + c_1 \cos\left[2\pi\left(\phi' - \phi_1'\right)\right] + c_2 \cos\left[4\pi\left(\phi' - \phi_2'\right)\right], \quad (1)$$

where $\phi' = \phi - \Delta\phi_{\rm ltd}$ is the orbital phase corrected for the light travel delay. The orbital phase is

$$\phi = \frac{t - T_0}{P} - n, \quad (2)$$

Table 3. Limb-darkening coefficients for WASP-121.

Exponent [i]	Ch1 (3.6 μm)	Ch2 (4.5 μm)
1/2	0.354241	0.341362
1	−0.134867	−0.211578
3/2	0.068047	0.150017
2	−0.017143	−0.045761

Notes. [i]Of the power term from the four-coefficient law (Claret 2000).

where T_0 is the epoch of transit, P is the orbital period, and n is an integer number usually chosen such that $-1 \le \phi \le 1$. The light travel delay accounts for the displacements of the planet along the line of sight with respect to inferior conjunction. For a circular orbit,

$$\Delta\phi_{\rm ltd} = \frac{a \sin i \left[1 - \cos\left(2\pi\phi\right)\right]}{cP}, \quad (3)$$

where a and i are the orbital semimajor axis and inclination, and c is the speed of light.

We adopted PYLIGHTCURVE[1] (Tsiaras et al. 2016) to model the occultations, which is based on the formalism from Pál (2008). We computed the stellar limb-darkening coefficients through ExoTETHyS[2] (Morello et al. 2020a,b), using spectral model grids from the PHOENIX library (Claret et al. 2012, 2013; Husser et al. 2013) and the so-called claret-4 parametrisation (Claret 2000). Table 3 reports the limb-darkening coefficients for both *Spitzer*/IRAC passbands.

3.4. Data fitting

We performed similar independent fits on both visits, taken separately. For each visit, we simultaneously fitted the light-curve model and instrumental systematic effects to the raw light curve, discarding the second AOR. For each AOR segment considered, we fit a linear combination of the light-curve model and

---

[1] https://github.com/ucl-exoplanets/pylightcurve
[2] https://github.com/ucl-exoplanets/ExoTETHyS

Table 4. Prior probability distributions of the fitted parameters.

Parameter (units)	Prior
p ( ) [i]	$\mathcal{U}(0, 1)$
P (days) [ii]	$\mathcal{N}(1.2749255, 2.5 \times 10^{-7})$
T_0 (HJD$_{\mathrm{TDB}}$) [iii]	$\mathcal{U}(2456635.54895, 2456635.86769)$
b ( ) [iv]	$\mathcal{U}(0, 1)$
T_{14} (h) [v]	$\mathcal{U}(0, 8.6616)$
a (au) [vi]	$\mathcal{N}(0.02544, 0.00050)$
c_0 ( ) [vii]	$\mathcal{U}(0, 1)$
c_1 ( ) [vii]	$\mathcal{U}(-1, 1)$
ϕ_1' ( ) [vii]	$\mathcal{U}(-0.5, 0.5)$
c_2 ( ) [vii]	$\mathcal{U}(-1, 1)$
ϕ_2' ( ) [vii]	$\mathcal{U}(-0.5, 0.5)$
N_{AOR} (MJy sr^{-1}) [viii]	$\mathcal{U}^3(0, 3000)$
k_{ICA} ( ) [ix]	$\mathcal{U}^{72}(-100, 100)$

Notes. $\mathcal{U}(a, b)$ denotes a uniform prior delimited by a and b; $\mathcal{N}(\mu, \sigma)$ denotes a normal prior with μ mean and σ width; literature values were taken from Delrez et al. (2016), alias D16. Parameters: [i]planet/star radius ratio, $p = R_{\mathrm{p}}/R_*$; [ii]orbital period, normal prior from D16; [iii]epoch of transit, uniform prior interval centred on D16 value with width equal to 0.25 P; [iv]impact parameter, $b = a \cos i / R_*$; [v]total transit duration from first to fourth contact, uniform prior interval from 0 to $3 \times$ D16 value; [vi]orbital semimajor axis, normal prior from D16; [vii]phase-curve parameters defined in Eq. (1); [viii]scaling factors for the light-curve model, independent for each AOR; [ix]scaling factors for the ICA components.

24 ICA components attributed to instrumental signals. The scaling factors for the light-curve model and the ICA components of different AORs were independent parameters. The astrophysical parameters were planet-to-star radius ratio (p), orbital period (P), epoch of transit (T_0), impact parameter (b), total transit duration (T_{14}), orbital semi-major axis (a), and five phase-curve parameters (as in Eq. (1)). These parameters were shared among the AORs of the same visit.

Table 4 reports the Bayesian priors assigned to the 86 free parameters listed above. We set large uniform priors for almost all parameters. The orbital period and semi-major axis are wavelength-independent parameters that are very well known from previous observations, for which we adopted normal priors based on the results from Delrez et al. (2016). We performed a preliminary optimisation using `scipy.optimize.minimize` with the Nelder–Mead method (Nelder & Mead 1965). The root mean square (rms) of the corresponding residuals was assigned as the error bar to each photometric point, which is typically larger than the nominal error bars. Then we ran emcee (Foreman-Mackey et al. 2019) with 300 walkers and 200 000 iterations. Each walker was initialised with a random value close to the preliminary parameter estimate. The first 50 000 iterations were discarded as burn-in.

3.5. Alternative fits

We tested fitting a phase-curve model with a single sinusoid, namely, fixing $c_2 = 0$ in Eq. (1). The corresponding results were not preferred, as explained in Sect. 4.1. We also tried fixing the geometric and orbital parameters to better constrain the difference in transit depth between IRAC passbands, as discussed in Sect. 4.2. These tests were not used to calculate the final parameters reported in Table 5.

4. Results

Figure 1 shows the best-fit models to the raw light curves and the corresponding residuals. The rms amplitudes of the normalised residuals are 2.45×10^{-3} for the 3.6 µm visit, and 2.81×10^{-3} for the 4.5 µm visit. We estimated them to be ~28.7% and 6.8% above the photon noise limit. Figure 3 shows the rms amplitudes of the binned residuals versus the bin size. The 4.5 µm residuals show no significant deviations from the theoretical behaviour of white noise. The 3.6 µm residuals present a modest amount of correlated noise, as is often the case for observations with this IRAC channel (e.g. Maxted et al. 2013; Stevenson et al. 2017; Zhang et al. 2018; Dang et al. 2022).

4.1. Model selection

We compared the phase-curve models with a single or double sinusoid, as described in Sects. 3.3–3.5. We considered the Bayesian information criterion (BIC; Schwarz 1978) and the Akaike information criterion (AIC; Akaike 1974) to guide our model selection. For the 3.6 µm observation, the double sinusoid is statistically preferred according to both criteria with ΔBIC = -52 and ΔAIC = -67. We note that $|\Delta$BIC$| > 10$ (or $|\Delta$AIC$| > 10$) indicates a very strong evidence in favour of either model, based on the scale by Raftery (1995). For the 4.5 µm observation, the analogous differences have opposite sign, ΔBIC = 18 and ΔAIC = 2.7, thus favouring the single sinusoid model. We note that $|\Delta$AIC$| \sim 2$ indicates a weak statistical preference for the model with the lowest AIC.

Finally, we selected the results obtained with the double sinusoid model for both observations. The choice to adopt the same parametrisation for both observations was taken to ensure homogeneity in their analyses. In fact, we expect the same physical phenomena to be present in observations of the same system at multiple wavelengths, albeit with different relative amplitudes and/or signal-to-noise ratios (S/Ns). Additionally, the double sinusoid parametrisation is more flexible and includes the single sinusoid as a special subcase. Even if the second sinusoid were superfluous to reproduce the 4.5 µm data, the fit should find a null amplitude ($c_2 \sim 0$) without biasing the other parameters.

Indeed, the fits with single and double sinusoid led to 1σ consistent results for the 4.5 µm observation, and slightly more conservative error bars by up to ~10% when using the more complete parametrisation. As expected, the differences between the two sets of results for the 3.6 µm observation are more significant, sometimes exceeding the 3σ level. The single sinusoid led to unphysical results for the 3.6 µm phase curve, such as a negative nightside flux within ~2σ. This issue is overcome by adopting the double sinusoid model.

4.2. Transit and phase-curve parameters

Table 5 reports the best-fit parameters and others derived from those. The corresponding corner plots are presented in Appendix A. The transit geometric and orbital parameters estimated independently from the two observations are consistent within 1σ. There is no evidence of different transit depths (p^2) at 3.6 and 4.5 µm within their error bars of 120–130 ppm. We also attempted to fit both light curves with fixed geometric and orbital parameters (b, P and a) to reduce their degeneracies with transit depth. When fixing the above parameters, the differential transit depth slightly increased from 60 to 100 ppm, which is still below the 1σ error bars.

Table 5. Posterior distributions of the fitted and derived parameters.

Parameter (units)	Ch1 (3.6 µm)	Ch2 (4.5 µm)
	Fitted	
p ( )	0.1228 ± 0.0005	0.1231 ± 0.0005
P (days)	$1.2749255 \pm 2.5 \times 10^{-7}$	$1.2749255 \pm 2.5 \times 10^{-7}$
T_0 (HJD$_{\mathrm{TDB}}$)	$2\,456\,635.7066 \pm 0.0003$	$2\,456\,635.7065 \pm 0.0003$
b ( )	$0.24^{+0.07}_{-0.10}$	$0.15^{+0.09}_{-0.10}$
T_{14} (h)	$2.926^{+0.016}_{-0.014}$	$2.909^{+0.014}_{-0.011}$
a (au)	0.02544 ± 0.00050	0.02544 ± 0.00050
	Derived (transit)	
p^2 ($\times 10^{-2}$)	1.508 ± 0.012	1.514 ± 0.013
a_0 ( )	3.71 ± 0.07	$3.79^{+0.03}_{-0.06}$
i (deg)	$86.2^{+1.6}_{-1.2}$	87.8 ± 1.4
	Derived (phase curve)	
$F_{\mathrm{day}}^{\mathrm{MAX}}$ ($\times 10^{-3}$)	4.23 ± 0.08	5.09 ± 0.09
$F_{\mathrm{night}}^{\mathrm{MIN}}$ ($\times 10^{-3}$)	0.05 ± 0.24	0.71 ± 0.27
$\Delta\phi_{\mathrm{day}}^{\mathrm{MAX}}$ (deg)	5.9 ± 1.6	$5.0^{+3.4}_{-3.1}$
$\Delta\phi_{\mathrm{night}}^{\mathrm{MIN}}$ (deg)	-31 ± 6	4.5 ± 2.9
$T_{\mathrm{day}}^{\mathrm{MAX}}$ (K)	2670^{+55}_{-40}	2700^{+70}_{-50}
$T_{\mathrm{night}}^{\mathrm{MIN}}$ (K)	710^{+270}_{-710}	1130^{+130}_{-160}
A_{b} ( )	$0.37^{+0.07}_{-0.09}$	$0.32^{+0.08}_{-0.10}$
ε ( )	$0.013^{+0.034}_{-0.013}$	$0.077^{+0.040}_{-0.034}$
$F(\phi' = 0.5)$ ($\times 10^{-3}$)	4.21 ± 0.08	5.08 ± 0.09
$F(\phi' = 0)$ ($\times 10^{-3}$)	0.22 ± 0.26	0.72 ± 0.27
$\bar{T}_{\mathrm{p}}(\phi' = 0.5)$ (K)	2665^{+55}_{-40}	2700^{+70}_{-50}
$\bar{T}_{\mathrm{p}}(\phi' = 0)$ (K)	810^{+360}_{-810}	1130^{+130}_{-160}
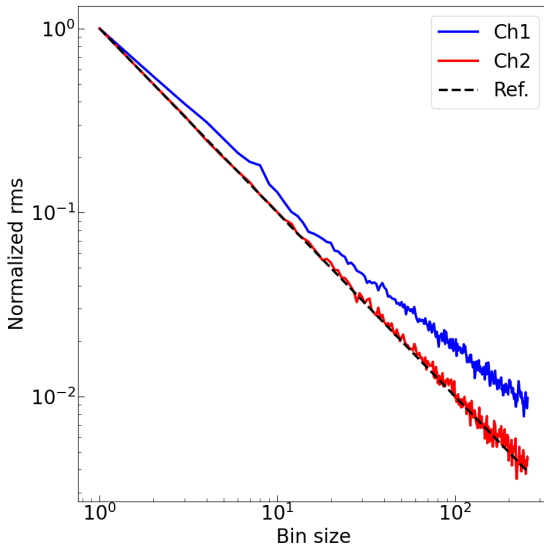
Fig. 3. Normalized rms of residuals as function of bin size for the 3.6 µm (blue) and 4.5 µm (red) visits. The unit bin size is 8 s. Depending on the bin size, a few points are discarded at the beginning of each AOR to avoid bins over the gaps between AORs. The black dashed line shows the theoretical behavior for Gaussian residuals.

From the posterior distributions of the phase-curve coefficients, we numerically calculated the dayside maximum and nightside minimum fluxes ($F_{\mathrm{day}}^{\mathrm{MAX}}$ and $F_{\mathrm{night}}^{\mathrm{MIN}}$) and their phase offsets from mid-transit and mid-eclipse time ($\Delta\phi_{\mathrm{day}}^{\mathrm{MAX}}$ and $\Delta\phi_{\mathrm{night}}^{\mathrm{MIN}}$). We used the `ExoTETHyS.BOATS` subpackage (Morello et al. 2021) to determine the brightness temperatures corresponding to the measured planetary fluxes. We obtained $F_{\mathrm{day}}^{\mathrm{MAX}} = (4.23 \pm 0.08) \times 10^{-3}$ and $(5.09 \pm 0.09) \times 10^{-3}$ at 3.6 and 4.5 µm, corresponding to similar brightness temperatures of $T_{\mathrm{day}}^{\mathrm{MAX}} = 2670^{+55}_{-40}$ and 2700^{+70}_{-50} K, respectively. The two phase-curve maxima occur with slight offsets after mid-eclipse, $\Delta\phi_{\mathrm{day}}^{\mathrm{MAX}} = 5°.9 \pm 1°.6$ and $5°.0^{+3.1}_{-3.4}$ at 3.6 and 4.5 µm, respectively. We could only place an upper limit of $F_{\mathrm{night}}^{\mathrm{MIN}} = (0.05 \pm 0.24) \times 10^{-3}$ on the 3.6 µm nightside minimum flux, corresponding to $T_{\mathrm{night}}^{\mathrm{MIN}} = 710^{+270}_{-710}$ K. We also measured $F_{\mathrm{night}}^{\mathrm{MIN}} = (0.71 \pm 0.27) \times 10^{-3}$ at 4.5 µm, corresponding to $T_{\mathrm{night}}^{\mathrm{MIN}} = 1130^{+130}_{-160}$ K. Following the formulation by Cowan & Agol (2011), we estimated the Bond albedo (A_{b}) and circulation efficiency (ε) from the brightness temperatures. We obtained $A_{\mathrm{b}} = 0.37^{+0.07}_{-0.09}$ and $\varepsilon = 0.013^{+0.034}_{-0.013}$ (3.6 µm), and $A_{\mathrm{b}} = 0.32^{+0.08}_{-0.10}$ and $\varepsilon = 0.077^{+0.040}_{-0.034}$ (4.5 µm).

5. Discussion

5.1. WASP-121 b atmosphere overview

The dayside emission spectrum of WASP-121 b, limited to the *Spitzer*/IRAC 3.6 and 4.5 µm passbands, is consistent with that
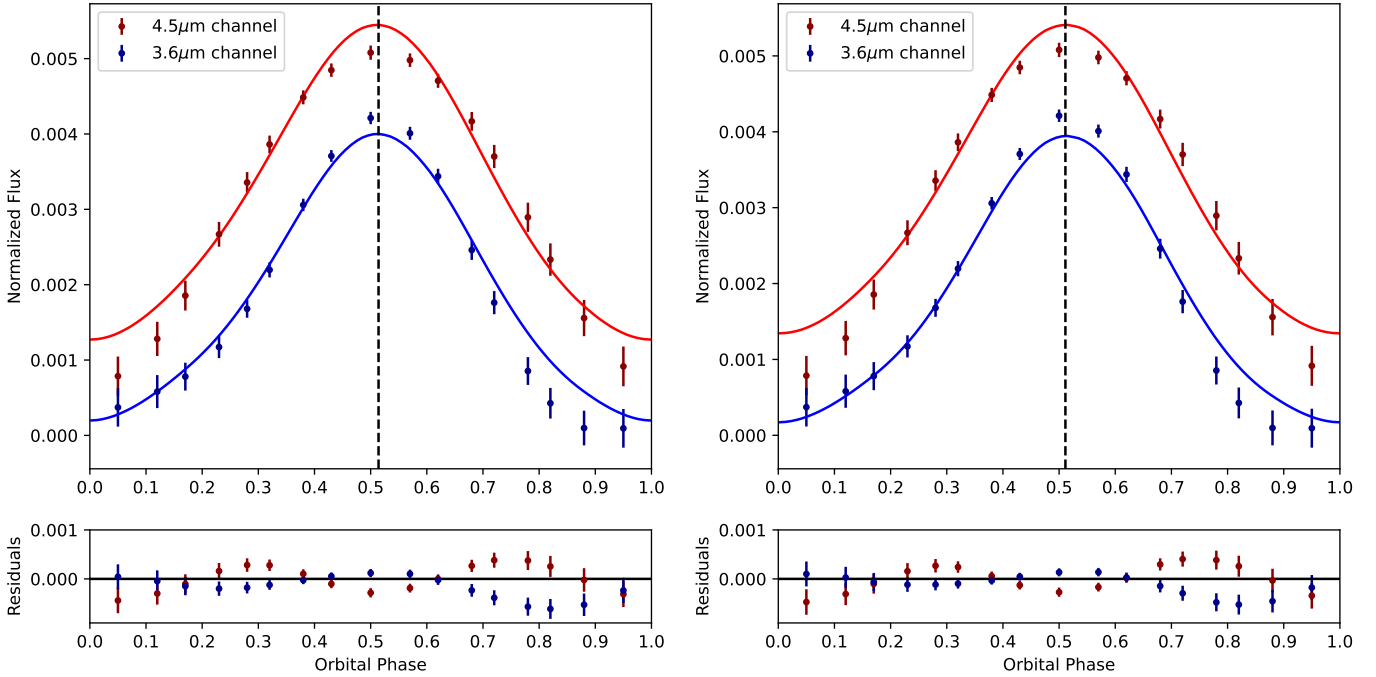
Fig. 4. Parametric *Spitzer* phase curves with error bars based on Eq. (1) and best-fit models from our 1.5D phase-curve retrieval. The dashed vertical lines indicate the position of the hot spot's centre. Note: the orbital phase has been corrected for the light travel delay, so that mid-eclipse occurs at $\phi' = 0.5$. Left: chemistry is fixed at $Z_p = 1\,Z_\odot$; Right: chemistry is fixed at $Z_p = 10\,Z_\odot$.

of a blackbody at 2680^{+60}_{-45} K (weighted average). The nightside emission is also consistent with that from a blackbody with 1100^{+165}_{-220} K. From this data, there is no evidence of molecular species either in emission (blackbody spectra) or in transmission (constant transit depths). The strong day-night contrast and small peak offsets point towards inefficient heat redistribution in the WASP-121 b atmosphere. Based on the weighted average blackbody temperatures, we report $\varepsilon = 0.07^{+0.05}_{-0.04}$. An interesting feature from both phase curves is the indication of a westward hot-spot offset, in the opposite direction to that predicted by most global circulation models (GCM) of hot Jupiter atmospheres (e.g. Showman & Guillot 2002; Showman et al. 2009; Perna et al. 2012; Mendonça et al. 2016; Deitrick et al. 2020). Although they are rare, westward hot-spot offsets have been previously reported for a few hot Jupiters (Armstrong et al. 2016; Dang et al. 2018; von Essen et al. 2020) and predicted theoretically (Rogers & Komacek 2014; Rogers 2017; Hindle et al. 2019).

We performed phase-curve retrievals with the phase-curve plugin (Changeat & Al-Refaie 2020; Changeat et al. 2021) of TauREx 3.1 (Al-Refaie et al. 2021, 2022), the latest version of the TauREx software (Waldmann et al. 2015a,b). For the atmosphere, we assumed three homogeneous regions: hot spot, dayside, and nightside. We computed the emitted flux at given phases using a quadrature integration scheme and fit all the phases for both channels in a single run. Each region is described by a plane-parallel atmosphere composed of 100 layers with pressures ranging from 10 to 10^{-6} bar in log scale. In principle, multiwavelength phase-curve observations may constrain the chemistry of exoplanet atmospheres (e.g. Stevenson et al. 2014; Kreidberg et al. 2018; Arcangeli et al. 2019), and thus potentially inform us about their formation and evolution pathways (e.g. Madhusudhan et al. 2014; Turrini et al. 2021; Cevallos Soto et al. 2022). However, the information content in regard to the chemistry is relatively low and is degenerate in *Spitzer* data, especially if the thermal structure is also unknown, so we

coupled the chemistry between the three regions of the planet and assumed chemical equilibrium. In the retrievals, the values for the metallicity (Z_p) and the carbon-to-oxygen (($C/O)_p$) ratio were left fixed. We tested runs with $Z_p = 1$–$10\,Z_\odot$ and with $(C/O)_p = 0.1$–1.0. The thermal profiles were described using a two-point profile with two freely moving nodes. In this model, the hot-spot region is defined by its location and size. We initially attempted to recover both parameters from the data but this led to nonphysical solutions. This issue may occur because with *Spitzer* data only, the hot-spot size is degenerate with the thermal structure. A similar behaviour was found and explored in more detail in Changeat et al. (2021); Changeat (2022), even when the HST data are combined with *Spitzer* data. We therefore fixed the hot-spot size to 40°, but left the hot-spot offset as a free parameter. For the nightside region, we modeled clouds using an opaque grey cloud model and fitted for the cloud pressure top deck. The parameter space of this phase-curve model was explored using the MultiNest algorithm (Feroz et al. 2009; Buchner 2016) with 512 live points and an evidence tolerance of 0.5. The priors were chosen to be uninformative, i.e., uniform priors with large bounds. More specifically, the hot-spot offset was allowed to vary between –50° and 50°, the temperature of the T-p nodes between 300 K and 6000 K, and the pressures of the T-p nodes as well as the top of the cloud deck were explored on the full extent of the atmosphere.

We show in Fig. 4 the *Spitzer* observations, calculated from the posterior distributions of our parametric fit based on Eq. (1), and two recovered best-fit atmospheric models. The corresponding retrieved thermal structures are shown in Fig. 5. While both runs indicate the likely presence of a thermal inversion, the altitude of the inversion cannot be inferred from this data as it is degenerate with the chemistry.

Analysing the posterior distributions (see Fig. A.3) of our atmospheric retrievals, we find that clouds are not required to explain the WASP-121 b *Spitzer* data. The hot-spot offset is
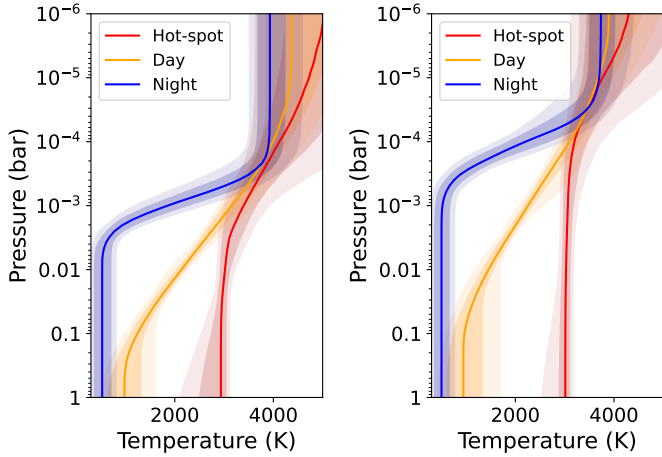
Fig. 5. Retrieved thermal structures for the $Z_p = 1 Z_\odot$ (left) and $Z_p = 10 Z_\odot$ (right) phase-curve retrievals, corresponding to the fits in Fig. 4. The shaded regions are the 1 and 3σ confidence levels. In both cases, a thermal inversion is needed to explain the data.

consistent between the two $Z_p = 1 Z_\odot$ and $Z_p = 10 Z_\odot$ retrievals, around 9° westward.

Looking at the residuals in Fig. 4, we note some discrepancies between our phase-curve models and *Spitzer* data. The anti-correlated behaviour of $3.6 \mu m$ and the $4.5 \mu m$ residuals suggest that the hot-spot offset, size, and temperature (shared in our retrievals) might be different between the two observations. This potential difference in the hot-spot parameters could be a consequence of atmospheric temporal variability or other effects that are not accounted for by our analysis, such as the observations probing different pressure regions, or remaining systematic biases from our data reduction. We defer further modelling efforts to future work, given the high level of complexity required to reproduce both observations and difficulty in constraining many atmospheric parameters using just two photometric observations.

5.2. Comparison with other observations of the same planet
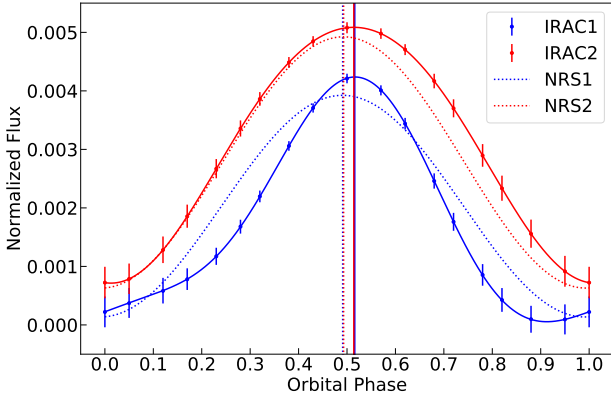
5.2.1. JWST/NIRSpec

The WASP-121 b phase curve was recently observed by JWST/NIRSpec using the G395H grating as part of program GO-1729 (P.I. Mikal-Evans, co-P.I. Kataria). This observing mode makes use of the NRS1 and NRS2 detectors, covering the 2.70–$3.72 \mu m$ and 3.82–$5.15 \mu m$ wavelength ranges. Mikal-Evans et al. (2023) presented the results of their first look analysis of the broadband light curves, integrated over each detector passband. We note that the NRS1 and NRS2 passbands largely overlap with those of *Spitzer*/IRAC channels 1 and 2, respectively. Hence, it makes sense to compare the results obtained from *Spitzer* and JWST observations.

Figure 6 shows the comparison between physical parameters from our *Spitzer*/IRAC data analysis and those based on the JWST/NIRSpec observations reported by Mikal-Evans et al. (2023). Figure 7 compares the corresponding phase-curve profiles. There is a good agreement between the two sets of parameters, albeit with larger error bars for the *Spitzer*/IRAC ones. In particular, the two-points dayside emission spectra of WASP-121 b inferred from *Spitzer*/IRAC or JWST/NIRSpec are both consistent with that of blackbodies. There is an apparent offset of ~ 80 K between the two sets of brightness temperatures, which is
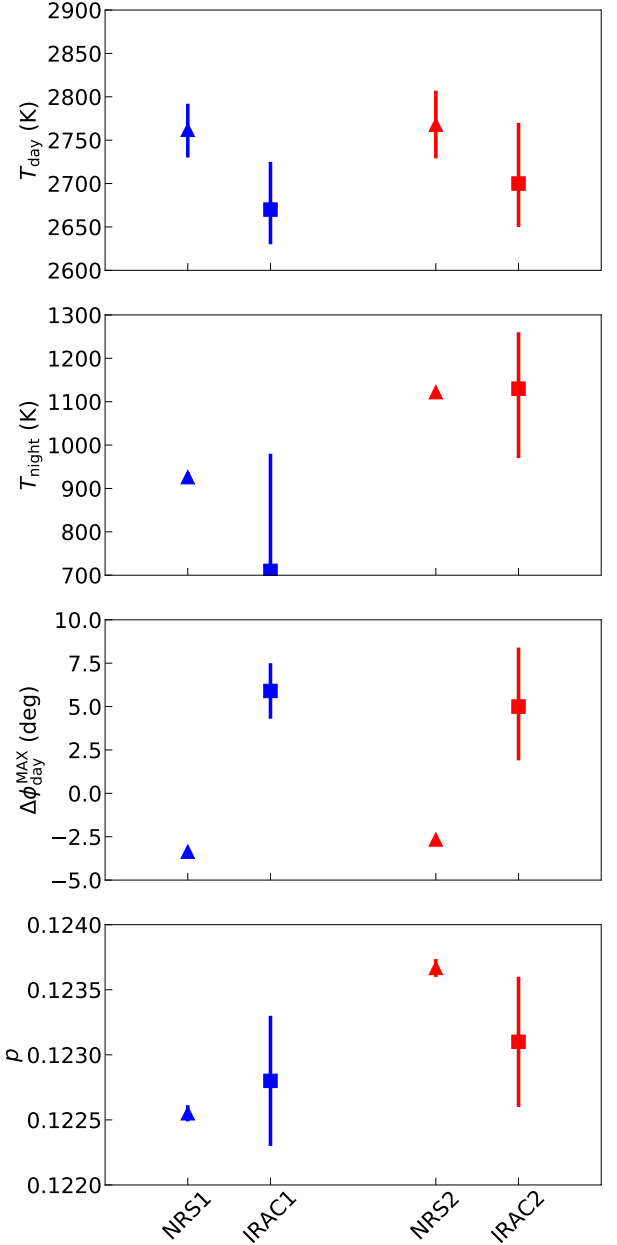
Fig. 6. Brightness temperatures inferred for the dayside (left panel) and nightside (right panel) of WASP-121 b, shown at the top. Offsets of the phase-curve maxima relative to conjunction (left panel), and planet-to-star radii ratios (right panel), shown at the bottom. Parameters obtained from the *Spitzer*/IRAC data are represented with blue and red squares for channel 1 and 2, respectively. Those obtained from the JWST/NIRSpec G395H data are represented with blue and red triangles for NRS1 and NRS2, respectively.

not statistically significant. The nightside temperatures reported for the *Spitzer*/IRAC and JWST/NIRSpec passbands have similar trends, the bluer temperatures being ~ 200–400 K lower than the redder. While the difference for the JWST/NIRSpec passbands is significant at the 12σ level, the statistical significance of the difference is decreased by the order-of-magnitude larger error bars for the *Spitzer*/IRAC measurements. The phase-curve maxima present different offsets from mid-eclipse, ranging from modest eastward to westward hot-spot positions for JWST/NIRSpec and *Spitzer*/IRAC measurements, respectively. The reported JWST/NIRSpec offsets are $3.36° \pm 0.11°$ (NRS1)

Fig. 7. Parametric phase-curve profiles for the *Spitzer*/IRAC observations analysed in this study (solid lines with error bars) and JWST/NIRSpec G395H inferred from Mikal-Evans et al. (2023; dotted lines). The vertical lines indicate the position of the maxima.

and 2.66° ± 0.12° (NRS2) prior to mid-eclipse. These differences may reveal the variable weather of WASP-121 b (Cho et al. 2003, 2021; Skinner & Cho 2022), or could be caused by instrumental systematic effects (Murphy et al. 2023). The planet-to-star radii ratios obtained in the *Spitzer*/IRAC passbands are consistent with the JWST/NIRSpec measurements within 1σ. The redder passbands have larger radii ratios at the 12σ level for JWST/NIRSpec. The *Spitzer*/IRAC measurements present a similar, but smaller, trend, that is not significant due to much larger error bars.

5.2.2. *Spitzer*/IRAC

Two other eclipses of WASP-121 b were observed with each of the *Spitzer*/IRAC channels in 2017, as part of the program ID 13044 (PI: Drake Deming). Garhart et al. (2020) reported lower dayside temperatures of 2490 ± 77 K (3.6 μm) and 2562 ± 66 K (4.5 μm) for WASP-121 b, based on those eclipse observations. The corresponding planet-to-star flux ratios reported by Garhart et al. (2020) are $(3.685 \pm 0.114) \times 10^{-5}$ and $(4.684 \pm 0.121) \times 10^{-5}$, which are smaller than our measurements by 545 and 406 ppm, respectively. These differences could be caused by the phase-blend effect (Martin-Lagarde et al. 2020), that was likely neglected by Garhart et al. (2020). We estimated this effect for the 4.5 μm eclipse using `ExoTETHyS.BOATS`, assuming the dayside and nightside temperatures reported in Table 5 and the 8.5-h duration of the *Spitzer* AORs. Indeed, the resulting phase-blend bias was –391 ppm, which is very similar to the discrepancy between the flux ratio reported by Garhart et al. (2020) and our value (–406 ppm).

5.2.3. HST/WFC3

Mikal-Evans et al. (2022) analysed two phase curves of WASP-121 b observed with HST/WFC3 using G141 grism, which are spectrally resolved over 1.1–1.7 μm. They reported dayside and nightside spectra with significant deviations from blackbody spectra, which they attributed to emission and absorption of H^- and H_2O. Nonetheless, they adopted the brightness temperatures derived from the blackbody fits for the dayside and nightside hemispheres to estimate the Bond albedo and circulation efficiency of WASP-121 b atmosphere, finding $A_b = 0.14 \pm 0.08$ and $\varepsilon = 0.29 \pm 0.02$. We calculated the corresponding brightness temperatures to be $T_{day} = 2760 \pm 100$ K

and $T_{night} = 1665 \pm 65$ K (not reported by Mikal-Evans et al. 2022). These HST/WFC3 observations suggest significantly lower Bond albedo, higher circulation efficiency and nightside temperatures than those that we obtained from *Spitzer*/IRAC observations. However, given the different wavelength ranges probed by HST and *Spitzer* observations, these apparent discrepancies do not necessarily reveal physical odds, but rather the limits of an oversimplified model behind these calculations.

Keating & Cowan (2017) pointed out that HST/WFC3 brightness temperatures can be overestimated due to neglecting the reflected star light component, namely, interpreting the observed flux from the planet dayside as pure emission. We calculated the reflected light component integrated over the HST/WFC3 G141 passband to be ∼92 ppm in eclipse, assuming a geometric albedo of 0.32 (equal to the Bond albedo from *Spitzer*/IRAC channel 2). Neglecting this component could bias the inferred dayside temperatures by about +50 K, but it should not affect the nightside temperature estimates.

Changeat et al. (2022) performed joint retrievals on a suite of emission and transmission spectra of WASP-121 b, based on *Spitzer*/IRAC and HST/WFC3 observations. They retrieved atmospheric temperatures, weighted by the contribution function, of 2602 ± 53 K for the dayside and 1386^{+340}_{-366} K for the terminator. We note that the terminator temperature is not informed by the nightside spectrum and should be intermediate between the dayside and nightside temperatures.

Concerning the phase-curve maxima, Mikal-Evans et al. (2022) found modest offsets ahead of mid-eclipse for HST/WFC3 broadband and spectroscopic light curves. Their posterior median for the broadband light-curve fit is $\Delta\phi^{MAX}_{day} \sim -6°$, in the opposite direction of our *Spitzer*/IRAC measurements.

5.2.4. TESS

The optical phase curve of WASP-121 b, as obtained from TESS data, has an amplitude of ∼400–500 ppm (Bourrier et al. 2020; Daylan et al. 2021). The former study found two solutions consistent with purely reflected starlight, leading to geometric albedo of ∼0.37, or pure thermal emission with $T_{day} = 2870 \pm 50$ K and $T_{night} < 2200$ K (3σ). The latter assumed pure thermal emission with a different stellar template from Stassun et al. (2019), leading to $T_{day} = 3012^{+40}_{-42}$ K and $T_{night} = 2022^{+44}_{-602}$ K. From the second set of results (Daylan et al. 2021), we calculated $A_b = 0.05^{+0.18}_{-0.22}$ and $\varepsilon = 0.40^{+0.17}_{-0.28}$. We note that infrared observations provide tighter constraints on the atmospheric thermal properties, thanks to their larger phase-curve amplitudes and less reflection. Even neglecting reflection, our *Spitzer*/IRAC error bars on A_b and ε are 2–8 times smaller than TESS ones.

5.3. Comparison with other planets

WASP-121 b belongs the class of UHJs, i.e., gas giants with dayside temperature $\gtrsim 2200$ K (Bell & Cowan 2018). This temperature is above the condensation threshold of most species, except highly refractory ones such as Al and Ti (Wakeford et al. 2017). For this reason, we may expect cloud-free dayside in UHJs (Helling et al. 2021). The lack of a reflecting cloud layer should also imply low geometric and Bond albedo ($\lesssim 0.2$), as confirmed by optical to near-infrared eclipse measurements (Mallonn et al. 2019). We estimated a higher Bond albedo of $\gtrsim 0.3$ from the *Spitzer*/IRAC phase curves of WASP-121 b at 3.6 and 4.5 μm, although their posteriors are consistent with $A_b = 0.2$ within 2σ. Schwartz & Cowan (2015) highlighted a common trend of

Table 6. Thermal phase-curve parameters of UHJs observed with *Spitzer*/IRAC.

Planet	Wavelength (μm)	T_{day} (K)	T_{night} (K)	$\Delta\phi_{\text{day}}^{\text{MAX}}$ (deg)	A_{b} ( )	ε ( )
WASP-19 b [i]	3.6	2384^{+41}_{-57}	890^{+280}_{-890}	-10.5 ± 4.0	$0.35^{+0.08}_{-0.09}$	$0.05^{+0.09}_{-0.05}$
	4.5	2357 ± 64	1130^{+240}_{-130}	-12.9 ± 3.6	$0.33^{+0.09}_{-0.11}$	$0.13^{+0.12}_{-0.05}$
HAT-P-7 b [i]	3.6	2632 ± 77	$<1360\ (2\sigma)$	6.8 ± 7.5	$0.18^{+0.16}_{-0.21}$	$<0.02\ (2\sigma)$
	4.5	2682 ± 49	1710 ± 180	4.1 ± 7.5	$-0.13^{+0.22}_{-0.29}$	$0.35^{+0.12}_{-0.11}$
WASP-76 b [ii]	3.6	2471 ± 27	1518 ± 61	-0.68 ± 0.48	$0.24^{+0.07}_{-0.08}$	0.31 ± 0.04
	4.5	2699 ± 32	1259 ± 44	-0.67 ± 0.20	0.05 ± 0.09	$0.117^{+0.017}_{-0.015}$
WASP-33 b [iii]	3.6	3082 ± 92	1952^{+125}_{-134}	-12.8 ± 5.8	$0.25^{+0.09}_{-0.10}$	0.34 ± 0.06
	4.5	3209^{+89}_{-87}	1498^{+114}_{-118}	-19.8 ± 3.0	$0.25^{+0.08}_{-0.09}$	0.12 ± 0.03
WASP-121 b [iv]	3.6	2670^{+55}_{-40}	710^{+270}_{-710}	5.9 ± 1.6	$0.37^{+0.07}_{-0.09}$	$0.013^{+0.034}_{-0.013}$
	4.5	2700^{+70}_{-50}	1130^{+130}_{-160}	$5.0^{+3.1}_{-3.4}$	$0.32^{+0.08}_{-0.10}$	$0.077^{+0.040}_{-0.034}$
KELT-1 b [v]	3.6	2988 ± 60	1173^{+175}_{-130}	-28.4 ± 3.5	$0.09^{+0.09}_{-0.10}$	$0.06^{+0.04}_{-0.02}$
	4.5	2902 ± 74	1053^{+230}_{-161}	-18.6 ± 5.2	$0.19^{+0.09}_{-0.10}$	$0.05^{+0.05}_{-0.02}$
WASP-103 b [vi]	3.6	2995 ± 159	1523 ± 153	-2.0 ± 0.7	$0.15^{+0.17}_{-0.21}$	$0.16^{+0.08}_{-0.06}$
	4.5	3154 ± 99	1288 ± 118	-1.0 ± 0.4	$0.02^{+0.15}_{-0.18}$	$0.07^{+0.03}_{-0.02}$
WASP-12 b [vii]	3.6	2744 ± 48	1510 ± 210	N.A.	$0.38^{+0.10}_{-0.12}$	$0.21^{+0.12}_{-0.09}$
	3.6	2813 ± 48	1760 ± 97	N.A.	$0.26^{+0.11}_{-0.13}$	0.33 ± 0.06
	4.5	2989 ± 66	790 ± 150	N.A.	$0.24^{+0.12}_{-0.14}$	$0.013^{+0.013}_{-0.007}$
	4.5	2854 ± 74	1340 ± 180	N.A.	$0.32^{+0.11}_{-0.13}$	$0.12^{+0.07}_{-0.05}$
KELT-9 b [viii]	4.5	4566^{+140}_{-136}	2556^{+101}_{-97}	$-18.7^{+2.1}_{-2.3}$	$0.29^{+0.14}_{-0.18}$	0.23 ± 0.04

Notes. The brightness temperatures and hot-spot offsets were extracted from the literature, and used to calculate the Bond albedo and circulation efficiency.
References. [i]Wong et al. (2016); [ii]May et al. (2021); [iii]Zhang et al. (2018); [iv]This work; [v]Beatty et al. (2019); [vi]Kreidberg et al. (2018); [vii]Bell et al. (2019); [viii]Mansfield et al. (2020).

measuring systematically higher Bond albedos from thermal phase curves of gas giants ($A_{\text{b}} \sim 0.35$) compared to the geometric albedos inferred from visible eclipses ($A_{\text{g}} \sim 0.1$). This trend holds, with a few exceptions, for more recent observations of UHJs (see Table 6).

The thermal phase curves of UHJs typically have large amplitudes, corresponding to strong day-night contrasts, and small hot-spot offsets. These properties indicate inefficient heat redistribution. We derived $\varepsilon \lesssim 0.1$ for most UHJs, the lowest values were obtained for WASP-121 b (see Table 6). There are no evident trends between the irradiation temperatures of UHJs and the observed thermal phase-curve parameters.

6. Conclusions

We analysed, for the first time, two thermal phase curves of WASP-121 b taken with *Spitzer*. Despite these datasets being affected by stronger than usual instrumental systematic effects, we obtained meaningful information on the exoplanet atmosphere. The measured brightness temperatures and transit depths are consistent within 1σ with those obtained from much more precise JWST observations in similar passbands. We estimated the Bond albedo and circulation efficiency of the WASP-121 b atmosphere, which are similar to those of other UHJs. However, we measured unusual westward hot-spot offsets, which are significantly different from the JWST measurements. These

discrepancies may hint at atmospheric variability or instrumental systematic effects. We further explored the possible thermal profiles using phase-curve retrievals, which are coupled with chemistry. Our analysis confirms the validity of *Spitzer* phase-curves to infer exoplanet atmospheric properties. More precise, spectrally resolved observations, such as those obtained with JWST, will enable us to better understand their complex behaviour.

References

Akaike, H. 1974, IEEE Trans. Automatic Control, 19, 716
Akinsanmi, B., Barros, S. C. C., Santos, N. C., et al. 2019, A&A, 621, A117
Al-Refaie, A. F., Changeat, Q., Waldmann, I. P., & Tinetti, G. 2021, ApJ, 917, 37
Al-Refaie, A. F., Changeat, Q., Venot, O., Waldmann, I. P., & Tinetti, G. 2022, ApJ, 932, 123
Arcangeli, J., Désert, J.-M., Parmentier, V., et al. 2019, A&A, 625, A136
Armstrong, D. J., de Mooij, E., Barstow, J., et al. 2016, Nat. Astron., 1, 0004
Azevedo Silva, T., Demangeon, O. D. S., Santos, N. C., et al. 2022, A&A, 666, A10
Beatty, T. G., Marley, M. S., Gaudi, B. S., et al. 2019, AJ, 158, 166
Bell, T. J., & Cowan, N. B. 2018, ApJ, 857, L20
Bell, T. J., Zhang, M., Cubillos, P. E., et al. 2019, MNRAS, 489, 1995
Ben-Yami, M., Madhusudhan, N., Cabot, S. H. C., et al. 2020, ApJ, 897, L5
Borsa, F., Allart, R., Casasayas-Barris, N., et al. 2021, A&A, 645, A24
Bourrier, V., Kitzmann, D., Kuntzer, T., et al. 2020, A&A, 637, A36
Buchner, J. 2016, Astrophysics Source Code Library [record ascl:1606.005]
Cabot, S. H. C., Madhusudhan, N., Welbanks, L., Piette, A., & Gandhi, S. 2020, MNRAS, 494, 363
Cevallos Soto, A., Tan, J. C., Hu, X., Hsu, C.-J., & Walsh, C. 2022, MNRAS, 517, 2285
Changeat, Q. 2022, AJ, 163, 106
Changeat, Q., & Al-Refaie, A. 2020, ApJ, 898, 155
Changeat, Q., Al-Refaie, A. F., Edwards, B., Waldmann, I. P., & Tinetti, G. 2021, ApJ, 913, 73
Changeat, Q., Edwards, B., Al-Refaie, A. F., et al. 2022, ApJS, 260, 3
Chapman, E., Abdalla, F. B., Harker, G., et al. 2012, MNRAS, 423, 2518
Cho, J. Y. K., Menou, K., Hansen, B. M. S., & Seager, S. 2003, ApJ, 587, L117
Cho, J. Y. K., Skinner, J. W., & Thrastarson, H. T. 2021, ApJ, 913, L32
Claret, A. 2000, A&A, 363, 1081
Claret, A., Hauschildt, P. H., & Witte, S. 2012, A&A, 546, A14
Claret, A., Hauschildt, P. H., & Witte, S. 2013, A&A, 552, A16
Cowan, N. B., & Agol, E. 2011, ApJ, 729, 54
Damiano, M., Morello, G., Tsiaras, A., Zingales, T., & Tinetti, G. 2017, AJ, 154, 39
Dang, L., Cowan, N. B., Schwartz, J. C., et al. 2018, Nat. Astron., 2, 220
Dang, L., Bell, T. J., Cowan, N. B., et al. 2022, AJ, 163, 32
Daubechies, I. 1992, Ten Lectures on Wavelets (Society for Industrial and Applied Mathematics)
Daylan, T., Günther, M. N., Mikal-Evans, T., et al. 2021, AJ, 161, 131
Deitrick, R., Mendonça, J. M., Schroffenegger, U., et al. 2020, ApJS, 248, 30
Delrez, L., Santerne, A., Almenara, J. M., et al. 2016, MNRAS, 458, 4025
Di Marcantonio, P., Morossi, C., Franchini, M., & Lehmann, H. 2019, AJ, 158, 161
Evans, T. M., Sing, D. K., Wakeford, H. R., et al. 2016, ApJ, 822, L4
Evans, T. M., Sing, D. K., Kataria, T., et al. 2017, Nature, 548, 58
Evans, T. M., Sing, D. K., Goyal, J. M., et al. 2018, AJ, 156, 283
Fazio, G. G., Hora, J. L., Allen, L. E., et al. 2004, ApJS, 154, 10
Feroz, F., Hobson, M. P., & Bridges, M. 2009, MNRAS, 398, 1601
Foreman-Mackey, D., Farr, W., Sinha, M., et al. 2019, J. Open Source Softw., 4, 1864
Fortney, J. J., Lodders, K., Marley, M. S., & Freedman, R. S. 2008, ApJ, 678, 1419
Garhart, E., Deming, D., Mandell, A., et al. 2020, AJ, 159, 137
Haar, A. 1910, Math. Ann., 69, 331
Hellard, H., Csizmadia, S., Padovan, S., Sohl, F., & Rauer, H. 2020, ApJ, 889, 66
Helling, C., Lewis, D., Samra, D., et al. 2021, A&A, 649, A44
Hindle, A. W., Bushby, P. J., & Rogers, T. M. 2019, ApJ, 872, L27
Hoeijmakers, H. J., Seidel, J. V., Pino, L., et al. 2020, A&A, 641, A123
Hubeny, I., Burrows, A., & Sudarsky, D. 2003, ApJ, 594, 1011
Husser, T. O., Wende-von Berg, S., Dreizler, S., et al. 2013, A&A, 553, A6
Hyvärinen, A. 2001, Independent Component Analysis, Adaptive and Learning Systems for Signal Processing, Communications, and Control (New York: John Wiley)
Ingalls, J. G., Krick, J. E., Carey, S. J., et al. 2016, AJ, 152, 44
IRAC Instrument & Instrument Support Teams 2021, IRAC Instrument Handbook, https://irsa.ipac.caltech.edu/data/SPITZER/docs/irac/iracinstrumenthandbook/
Keating, D., & Cowan, N. B. 2017, ApJ, 849, L5
Kipping, D. M. 2010, MNRAS, 408, 1758

Kovács, G. & Kovács, T. 2019, A&A, 625, A80
Kreidberg, L., Line, M. R., Parmentier, V., et al. 2018, AJ, 156, 17
Madhusudhan, N., Amin, M. A., & Kennedy, G. M. 2014, ApJ, 794, L12
Maino, D., Farusi, A., Baccigalupi, C., et al. 2002, MNRAS, 334, 53
Maino, D., Donzelli, S., Banday, A. J., Stivoli, F., & Baccigalupi, C. 2007, MNRAS, 374, 1207
Mallonn, M., Köhler, J., Alexoudi, X., et al. 2019, A&A, 624, A62
Mansfield, M., Bean, J. L., Stevenson, K. B., et al. 2020, ApJ, 888, L15
Martin-Lagarde, M., Morello, G., Lagage, P.-O., Gastaud, R., & Cossou, C. 2020, AJ, 160, 197
Maxted, P. F. L., Anderson, D. R., Doyle, A. P., et al. 2013, MNRAS, 428, 2645
May, E. M., Komacek, T. D., Stevenson, K. B., et al. 2021, AJ, 162, 158
Mendonça, J. M., Grimm, S. L., Grosheintz, L., & Heng, K. 2016, ApJ, 829, 115
Merritt, S. R., Gibson, N. P., Nugroho, S. K., et al. 2020, A&A, 636, A117
Merritt, S. R., Gibson, N. P., Nugroho, S. K., et al. 2021, MNRAS, 506, 3853
Mikal-Evans, T., Sing, D. K., Goyal, J. M., et al. 2019, MNRAS, 488, 2222
Mikal-Evans, T., Sing, D. K., Kataria, T., et al. 2020, MNRAS, 496, 1638
Mikal-Evans, T., Sing, D. K., Barstow, J. K., et al. 2022, Nat. Astron., 6, 471
Mikal-Evans, T., Sing, D. K., Dong, J., et al. 2023, ApJ, 943, L17
Morello, G. 2015, ApJ, 808, 56
Morello, G., Waldmann, I. P., Tinetti, G., et al. 2014, ApJ, 786, 22
Morello, G., Waldmann, I. P., Tinetti, G., et al. 2015, ApJ, 802, 117
Morello, G., Waldmann, I. P., & Tinetti, G. 2016, ApJ, 820, 86
Morello, G., Danielski, C., Dickens, D., Tremblin, P., & Lagage, P. O. 2019, AJ, 157, 205
Morello, G., Claret, A., Martin-Lagarde, M., et al. 2020a, J. Open Source Softw., 5, 1834
Morello, G., Claret, A., Martin-Lagarde, M., et al. 2020b, AJ, 159, 75
Morello, G., Zingales, T., Martin-Lagarde, M., Gastaud, R., & Lagage, P.-O. 2021, AJ, 161, 174
Morello, G., Dyrek, A., & Changeat, Q. 2022, MNRAS, 517, 2151
Murphy, M. M., Beatty, T. G., Roman, M. T., et al. 2023, AJ, 165, 107
Nelder, J. A., & Mead, R. 1965, Comput. J., 7, 308
Pál, A. 2008, MNRAS, 390, 281
Parmentier, V., Line, M. R., Bean, J. L., et al. 2018, A&A, 617, A110
Perna, R., Heng, K., & Pont, F. 2012, ApJ, 751, 59
Raftery, A. E. 1995, Sociol. Methodol., 25, 111
Ricker, G. R., Winn, J. N., Vanderspek, R., et al. 2014, SPIE Conf. Ser., 9143, 914320
Rodríguez-Montoya, I., Sánchez-Argüelles, D., Aretxaga, I., et al. 2018, ApJS, 235, 12
Rogers, T. M. 2017, Nat. Astron., 1, 0131
Rogers, T. M., & Komacek, T. D. 2014, ApJ, 794, 132
Salz, M., Schneider, P. C., Fossati, L., et al. 2019, A&A, 623, A57
Schwarz, G. 1978, Ann. Stat., 6, 461
Schwartz, J. C., & Cowan, N. B. 2015, MNRAS, 449, 4192
Showman, A. P., & Guillot, T. 2002, A&A, 385, 166
Showman, A. P., Fortney, J. J., Lian, Y., et al. 2009, ApJ, 699, 564
Sing, D. K., Lavvas, P., Ballester, G. E., et al. 2019, AJ, 158, 91
Skinner, J. W., & Cho, J. Y. K. 2022, MNRAS, 511, 3584
Stassun, K. G., Oelkers, R. J., Paegert, M., et al. 2019, AJ, 158, 138
Stevenson, K. B., Désert, J.-M., Line, M. R., et al. 2014, Science, 346, 838
Stevenson, K. B., Line, M. R., Bean, J. L., et al. 2017, AJ, 153, 68
Tichavsky, P., KoldovskÃœ, Z., Yeredor, A., Gomez-Herrero, G., & Doron, E. 2008, IEEE Trans. Neural Netw., 19, 421
Tsiaras, A., Waldmann, I. P., Rocchetto, M., et al. 2016, ApJ, 832, 202
Tsiaras, A., Waldmann, I. P., Zingales, T., et al. 2018, AJ, 155, 156
Turrini, D., Schisano, E., Fonte, S., et al. 2021, ApJ, 909, 40
von Essen, C., Mallonn, M., Borre, C. C., et al. 2020, A&A, 639, A34
Wakeford, H. R., Visscher, C., Lewis, N. K., et al. 2017, MNRAS, 464, 4247
Waldmann, I. P. 2012, ApJ, 747, 12
Waldmann, I. P. 2014, ApJ, 780, 23
Waldmann, I. P., Tinetti, G., Deroo, P., et al. 2013, ApJ, 766, 7
Waldmann, I. P., Rocchetto, M., Tinetti, G., et al. 2015a, ApJ, 813, 13
Waldmann, I. P., Tinetti, G., Rocchetto, M., et al. 2015b, ApJ, 802, 107
Wang, J., Xu, H., Gu, J., et al. 2010, ApJ, 723, 620
Wang, J., Xu, H., An, T., et al. 2013, ApJ, 763, 90
Wong, I., Knutson, H. A., Kataria, T., et al. 2016, ApJ, 823, 122
Wu, X., Roby, T., & Ly, L. 2010, SPIE Conf. Ser., 7737, 773716
Zhang, M., Knutson, H. A., Kataria, T., et al. 2018, AJ, 155, 83

Appendix A: Corner plots

Figures A.1 and A.2 show the corner plots with the posterior distributions of astrophysical parameters obtained from the $3.6\,\mu m$ and $4.5\,\mu m$ observations, respectively. Figure A.3 shows the corner plots for the atmospheric parameters retrieved from both observations assuming $Z_p = 1\,Z_\odot$ and $Z_p = 10\,Z_\odot$.
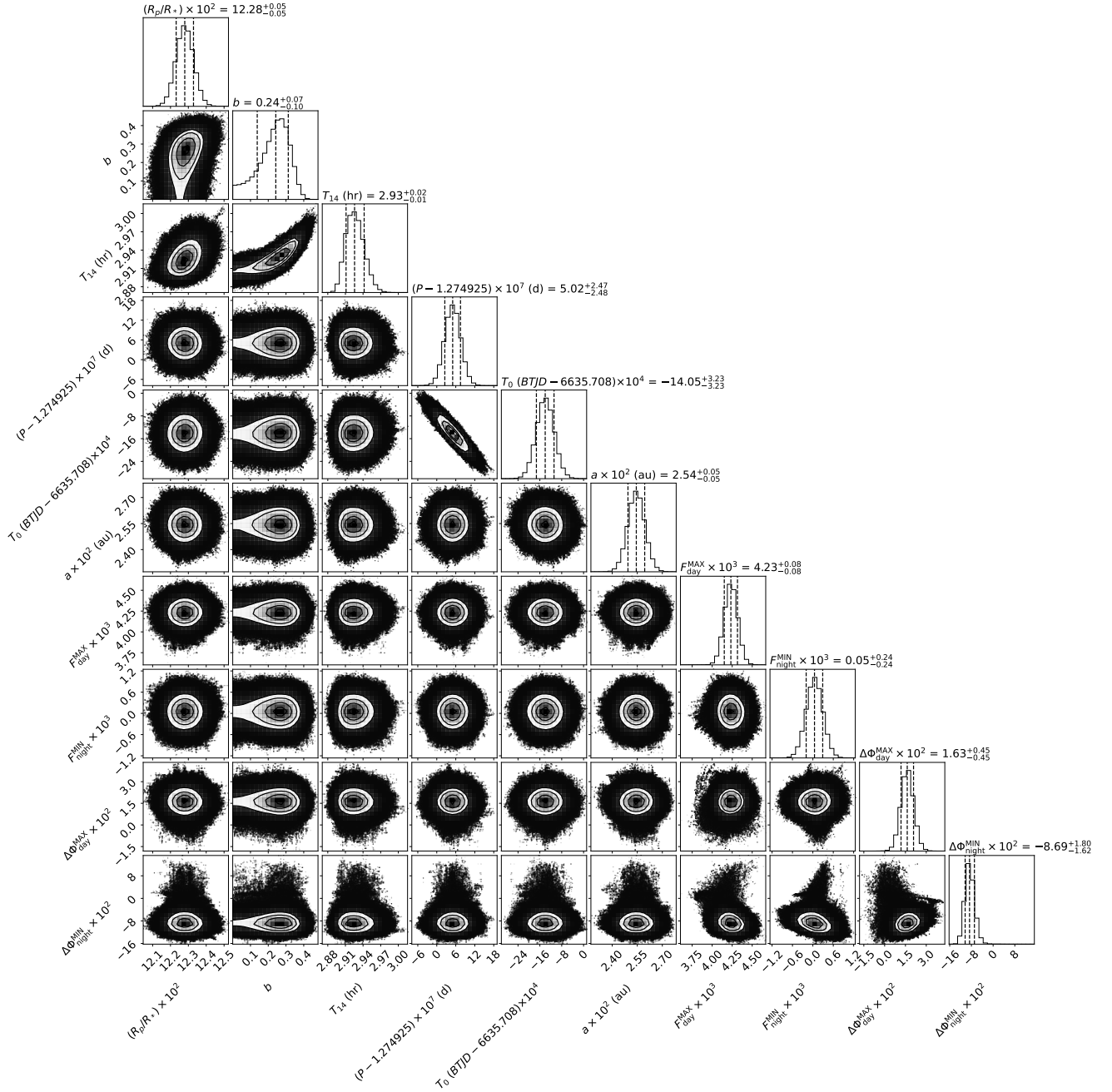
Fig. A.1. Posterior distributions of the light-curve fitting performed on the *Spitzer*/IRAC channel 1 data.
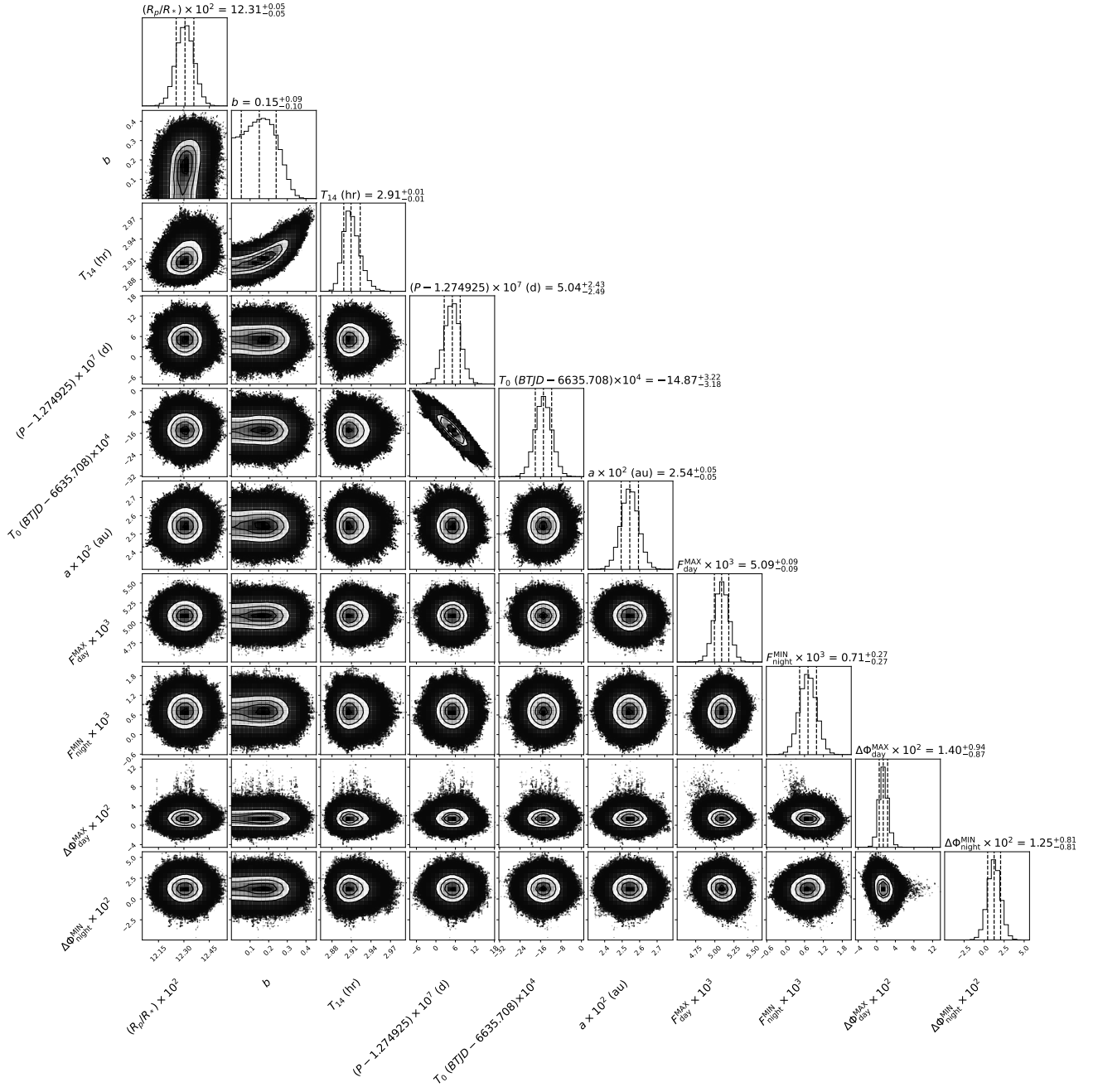
Fig. A.2. Posterior distributions of the light-curve fitting performed on the *Spitzer*/IRAC channel 2 data.
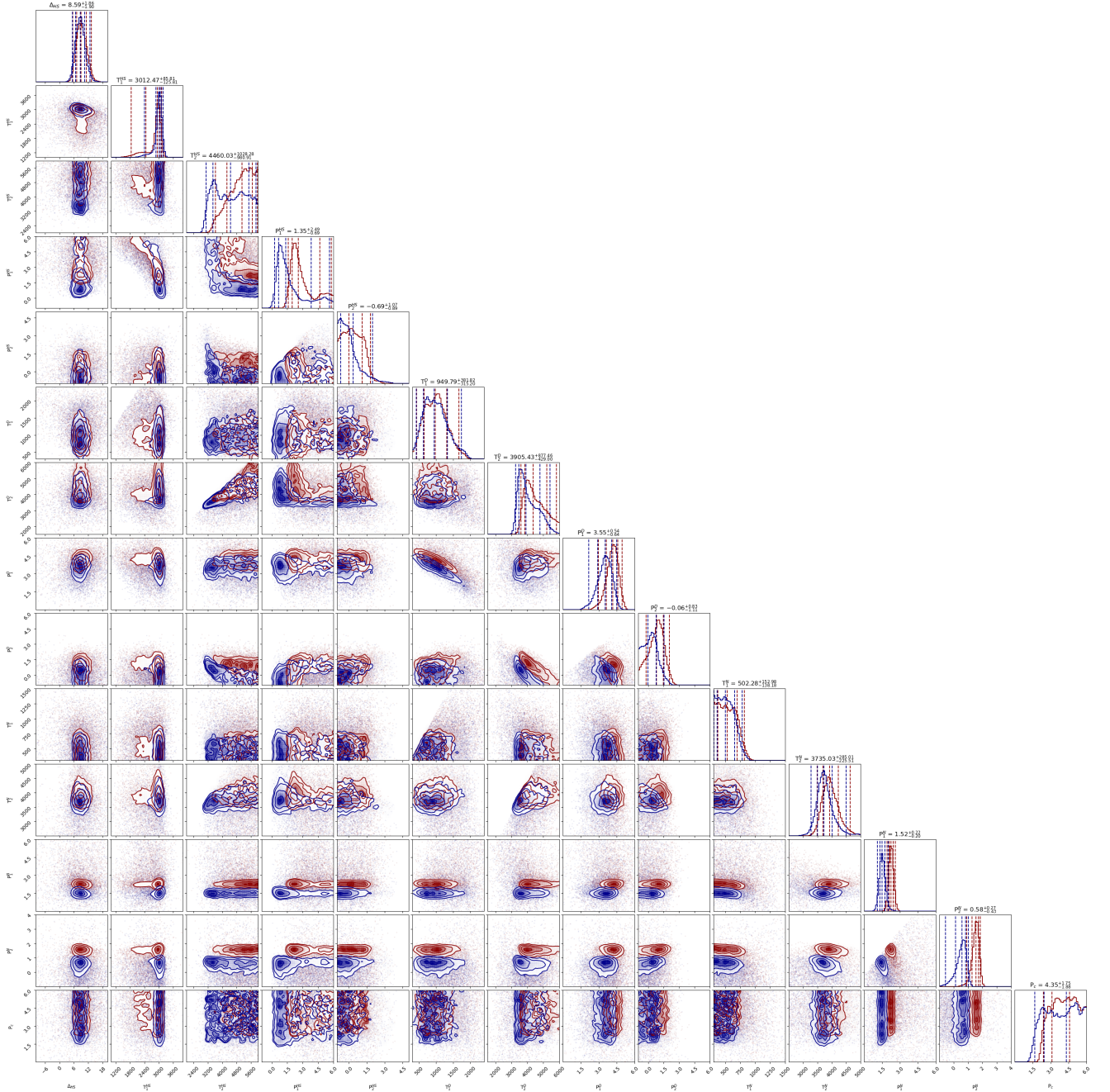
Fig. A.3. Posterior distributions of the atmospheric retrievals performed on the *Spitzer* data. Blue: retrieval with $Z_p = 1\,Z_\odot$; Red: Retrieval with $Z_p = 10\,Z_\odot$. Δ_{HS} is the hot-spot offset of the mode. HS: Hot-spot. D: Day. N: Night. P_c is the top pressure of the cloud deck.